American Mineralogist, Volume 76, pages 1662–1673, 1991

Geochemistry and mineralogy of fumarolic deposits, Valley of Ten Thousand Smokes, Alaska: Bulk chemical and mineralogical evolution of dacite-rich protolith

J. J. Papike
Institute of Meteoritics, Department of Geology, University of New Mexico, Albuquerque, New Mexico 87131, U.S.A.
T.E.C. Keith
U.S. Geological Survey, MS 910, Menlo Park, California 94025, U.S.A.
M. N. Spilde
Institute of Meteoritics, Department of Geology, University of New Mexico, Albuquerque, New Mexico 87131, U.S.A.
K. C. Galbreath
Combustion and Environmental Systems Research Institute, Energy and Environmental Research Center, University of North Dakota, Box 8213, University Station, Grand Forks, North Dakota 58202, U.S.A.
C. K. Shearer
Institute of Meteoritics, Department of Geology, University of New Mexico, Albuquerque, New Mexico 87131, U.S.A.
J. C. Laul
Rocky Flats, EG&G, P.O. Box 464, Golden, Colorado 80402, U.S.A.

Abstract

Samples from a fossil fumarole originating in the 1912 ash-flow tuff in the Valley of Ten Thousand Smokes have been analyzed to ascertain chemical changes resulting from high-temperature fumarolic alteration and subsequent cooling and weathering of the protolith. Samples of the underlying, dominantly leached, dacite-rich portion of the ash-flow tuff adjacent to the fumarolic conduit and samples of encrusted fallout from the shallow part of the fossil fumarole were interpreted using the isocon method of Grant (1986). The results show that, relative to unaltered 1912 dacite, chosen as a standard composition for the protolith in this fossil fumarole, mass was conserved during the alteration reactions for most of the system, but mass gains of 14–20% were determined for three samples in the leached ash-flow tuff. Relative to unaltered dacite protolith, significant enrichments occurred in SO_3, LOI ($\sim H_2O$), Cl, F, Zn, Pb, Cu, Sn, Cr, Ni, As, Sb, Au, Br in various parts of the fossil fumarole. Some of these were during the high-temperature part of the alteration, and some were during cooling processes when acid alteration becomes prominent. The REEs indicate some depletion in highly altered samples relative to dacite protolith and differential mobility of Eu^{2+} relative to trivalent REEs. This is manifested by positive Eu anomalies in REE patterns normalized against REE in the dacite protolith.

Mineral phases introduced in the alteration assemblages include alunite reflecting high SO_3 activity, hydrated aluminum hydroxy-fluoride (a ralstonite-like phase) and fluorite reflecting high F activity, smectite, magnetite, hematite, and goethite reflecting oxidation and hydration reactions. Opal and a portion of the α-cristobalite reflect SiO_2 mobility; however, the abundance of α-cristobalite is formed from pumice leached during high-temperature vapor-phase processes and devitrification of the altered glass.

Introduction

Spectacular fumaroles developed in the ash-flow sheet emplaced during the 6–8 June 1912 eruption from Novarupta, causing Robert F. Griggs, who discovered the steaming valley in 1916, to name the Valley of Ten Thousand Smokes (VTTS) (Griggs, 1922). Early studies of the active fumaroles of VTTS were reported by Shipley (1920), Allen and Zies (1923), and Zies (1929). Fumarole temperatures as high as 645 °C were recorded in 1919 (Allen and Zies, 1923), and these have cooled dramatically since initial activity. Ramdohr (1962) studied samples of newly deposited magnetite collected in 1919 from fumarole 148 of Zies (Allen and Zies, 1923) in the mid-valley region using reflected light, and he documented a variety of microscopic sulfides included in the magnetite. Lovering (1957) conducted a geochemical study on a suite of samples from fumarole no. 1 of Zies (Allen and Zies, 1923), in which he concluded that halogen-acid alteration differs from S-acid alteration chiefly in the greater loss of silica relative to alumina. Keith (1983, 1984, 1991) interpreted the origin and distribution of fumaroles in the VTTS, in

0003–004X/91/0910–1662$02.00

part drawing upon observations of Allen and Zies (1923). Heat to generate and sustain fumaroles was provided by the ash-flow sheet. Abundant meteoric H_2O flowing into and over the ash-flow sheet helped sustain the fumaroles and also hastened their cooling. The fumarolic fluids also included exsolved magmatic gases (Allen and Zies, 1923). Most of the fumaroles cooled and died out by the mid-1930s except in the Novarupta vent region, where residual fumaroles remain with temperatures as hot as 90 °C (Keith, 1991).

We have initiated a project to study the geochemistry and mineralogy of the VTTS fossil fumaroles (Papike et al., 1989, 1990a, 1990b, 1990c, 1991). Our major objectives are to (1) assess chemical losses and gains in ash-flow and fallout deposits that host the fumaroles, (2) determine mineralogical changes and reaction paths, and (3) determine chemical and crystal-chemical aspects of phenocryst alteration. This paper describes the bulk chemical and mineralogical evolution of a well-exposed, typical fossil fumarole (site 212) in the midvalley region (Fig. 1).

Studies of deposits at active fumaroles in other parts of the world (e.g., Stoiber and Rose, 1974; Symonds et al., 1987, 1990; Quisefit et al., 1989; Kodosky and Keskinen, 1990) have greatly increased our understanding of the geochemistry and mineralogy of these complex deposits. In contrast, our studies of VTTS fossil fumaroles do not provide as simple a picture of the processes operative in fumaroles as these referenced studies but instead characterize ejecta that have been subjected not only to high-temperature fumarolic activity but also to alteration during cooling and weathering (Keith, 1991). The samples we are studying represent an integated history of process and time as depicted schematically in Figure 2.

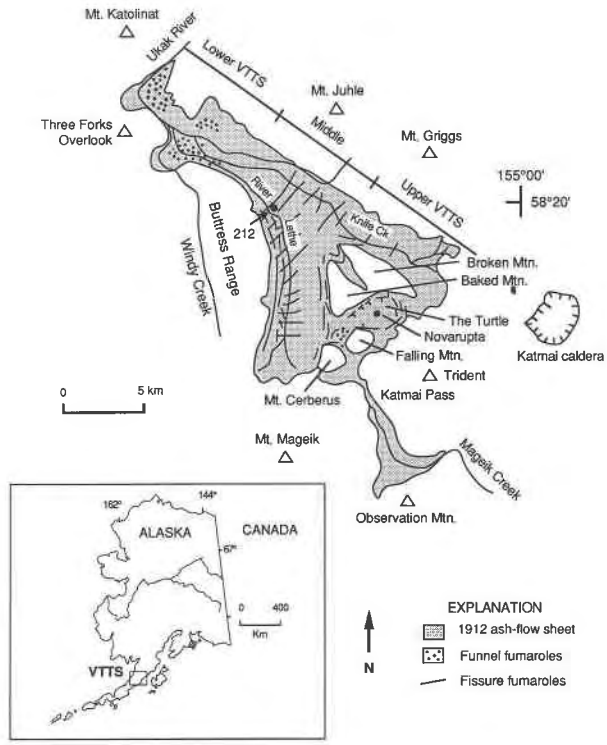

Fig. 1. Location map of Valley of Ten Thousand Smokes (VTTS), Alaska, (insert) and schematic map showing distribution of the 1912 ash-flow sheet and location of fumarole 212; modified from Keith (1991).

Geologic setting

The 1912 eruption of Novarupta in the Katmai region (Fig. 1) is regarded by many as the outstanding igneous event of this century (Eichelberger and Hildreth, 1986). During June 6–8, 1912, approximately 12 km³ of magma erupted from the Novarupta vent at the head of the Valley of Ten Thousand Smokes (VTTS), Alaska, producing ~17 km³ of fallout, 11 ± 4 km³ of ash-flow tuff, and ~1 km³ of heterogeneous proximal fallout within ~60 h (Hildreth, 1983, 1987, 1990). Curtis (1968) first separated out the 1912 eruptive stratigraphy and described the fallout deposits as A–H layers, and Hildreth (1983) presented detailed initial petrologic studies of the 1912 deposits. Initial composition of the ash-flow sheet was rhyolite (77% SiO_2), and increasing amounts of dacite (66–64.5% SiO_2) and andesite (61.5–58.5% SiO_2) were introduced later in the eruptive sequence (Hildreth, 1983). The exposures of the ash-flow sheet presently filling the VTTS are rhyolite rich and nonwelded at the distal end ~15–20 km from the vent; exposures in the middle and upper VTTS are sintered and consist of varying proportions of rhyolite, dacite, and andesite with minor amounts of banded pumice and lithic fragments (Hildreth, 1983; Fierstein and Hildreth, in preparation). Andesitic scoria is common in the near-vent, thin ash-flow layers and fallout. Maximum thickness of the ash-flow tuff is unknown but is likely ~200 m in the upper River Lethe area and almost as thick in the upper Knife Creek area (Curtis, 1968; Kienle, 1970).

Phenocrysts of plagioclase, orthopyroxene, titanomagnetite, ilmenite, and trace amounts of apatite and pyrrhotite are present in all pumice compositions, although rhyolitic pumice has only 1–2% total phenocryst content and dacite and andesite may have as much as 45% (Hildreth, 1983). Clinopyroxene is common in dacite and andesite; quartz and scarce amphibole occur in rhyolite; andesite contains scarce olivine (Hildreth, 1983). The initial fall unit underlying the ash-flow sheet is 100% rhyolite, fall unit B on top of the ash-flow tuff is mixed upward with increasing dacite and andesite relative to rhyolite, and fall units C–H on top of the ash flows are >98% dacite (Fierstein and Hildreth, 1990, and in preparation).

Configuration and distribution of fumaroles throughout the VTTS was controlled by the degree of welding of the ash-flow sheet, which in turn controlled fracturing and permeability (Keith, 1991). Hotter, longer-lived fumaroles occurred in the upper VTTS closer to the vent where the ash-flow sheet was thicker, more indurated, and more mafic (dacite and andesite) in contrast to thinner nonwelded rhyolitic tuff in the distal part of the ash-

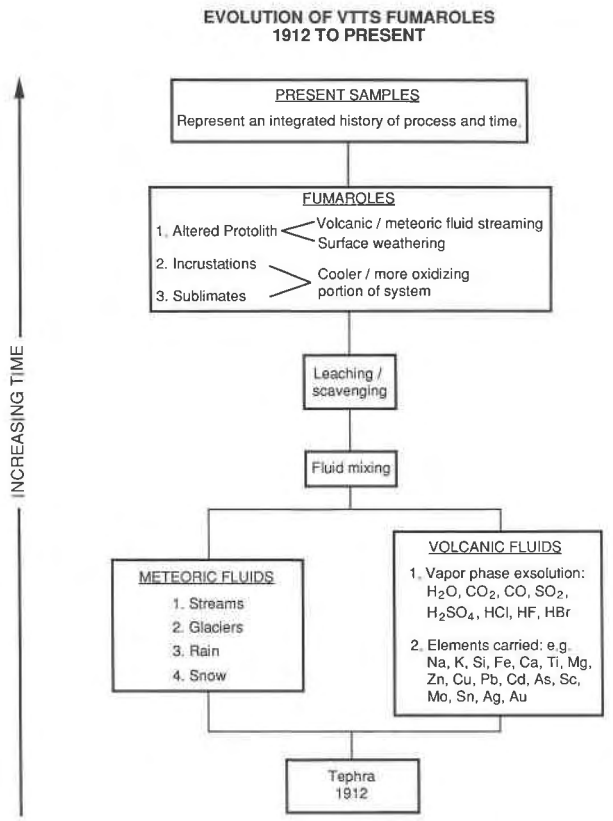

Fig. 2. Diagram illustrating the processes involved in fossil fumarole development and thus the mineralogical and geochemical complexity of the fossil fumaroles in the VTTS.

flow sheet. The distribution of high-temperature fumaroles prevalent in the middle and upper VTTS was controlled by fractures in the ash-flow sheet.

Keith (1991) determined that high-temperature fossil fumarolic incrustations exposed in the VTTS consist mostly of fall deposits encrusted mainly with either magnetite or hematite depending on f_{O_2} and temperature of deposition. Hematite and goethite also formed from altered magnetite during cooling processes. Fumarolically deposited α-cristobalite coexists with magnetite in high-temperature fossil fumaroles. The outer, cooler parts of a fossil fumarole typically have a relatively impermeable shell consisting of several of the following minerals: alunite, AHF (hydrated aluminum hydroxy-fluoride, a ralstonite-like phase described by Desborough and Rostad, 1980), fluorite, α- and β-cristobalite, opal, pyrite, S, kaolinite, illite, goethite, and amorphous hydrous Fe oxide (limonite). A large volume of unstable fumarolic deposits were removed by dissolution while the fumaroles were active (Keith, 1991).

The fumarole selected for this study is part of an extinct high-temperature, fissure fumarole (Keith, 1991) exposed on the northeast side of River Lethe in the midvalley region (Fig. 1). The upper 2 m of the ash-flow sheet at the fumarole site is composed mainly of dacite with subordinate amounts of andesite, rhyolite, banded pumice, and lithic fragments (Hildreth, 1983; Fierstein and Hildreth, unpublished pumice count data, 1991). Below 2 m in the ash-flow sheet, the composition decreases in amount of dacite and increases in amounts of andesite and rhyolite (Hildreth, 1983). The fall deposits overlying the ash-flow sheet at fumarole 212 are of mixed andesite, dacite, and rhyolite at the base and grade quickly upward into >98% dacite (Curtis, 1968; Hildreth, 1983; Fierstein and Hildreth, 1990).

A vertical joint in the ash-flow sheet was the fumarolic conduit for vigorously rising, hot fluids that leached and sintered the adjacent tuff in the deeper parts of the fumarolic system (Keith, 1991). Upon contact with the loose, permeable fallout overlying the ash-flow sheet, a state of disequilibrium was caused by rapid cooling and changes in gas fugacities that resulted in sublimation of mineral components carried in the vapor phase, forming incrustations on fallout clasts. Other chemical components were transported into the atmosphere. Depending on proximity to the hot fumarolic fluids, various states of alteration of the ash-flow sheet and fall deposits occur. Phenocrysts and pumice clasts in the fall deposits were partly shielded from fumarolic alteration where fumarolic minerals enclosed the clasts and where the clasts were not in the main path of hot, rising fumarolic fluids. Alteration during subsequent cooling, particularly that caused by the condensation of fumarolic fluids and mixing of fumarolic gases with surface H_2O at the upper and outer parts of the fumarole, resulted in acid alteration of both primary tephra and earlier deposited fumarolic minerals.

Samples for the present study are bulk samples, consisting of large fist-sized pieces of the altered ash-flow tuff and golfball-sized pieces of encrusted fallout, that were collected systematically from the leached and depositional parts of the fumarolic system (Fig. 3). The ash-flow tuff is leached progessively less away from the fumarole conduit (Fig. 3b); sample J is adjacent to the conduit and is the most leached, whereas sample O is the farthest from the conduit and was expected to be unaltered. Samples A through H (Fig. 3a) are from dacite-rich fall deposits encrusted with fumarolic minerals. Samples A and B are from the outer, cooler part of the encrusted fallout and C through H are from the inner part near the conduit where fumarolic gases reached the surface.

Sample preparation and analytical methods

Powders for X-ray diffraction (XRD), X-ray fluorescence (XRF), and instrumental neutron activation analysis (INAA) were prepared in a Spex hardened steel ball mill, with XRD powders being further ground by hand to approximately 10 μm in a ceramic mortar and pestle. Powders for Fe^{2+}/Fe^{3+} determinations were ground in a corundum mortar. Samples for F analysis were powdered in a Spex hardened steel puck mill.

Whole-rock powders were analyzed for major oxides and trace elements by energy dispersive X-ray fluores-

cence (EDXRF) and atomic absorption spectroscopy (AAS) at Battelle, Pacific Northwest Laboratories, Richland, Washington. Analyses of U.S. Geological Survey standards AGV-1, BCR-1, and G-2 (Flanagan, 1967, 1969, 1973) indicate precisions of better than 3% for Si, Ti, Al, Fe, Mg, Ca, K, and Zn; 5% for Na, V, Y, and Pb; 10% for Mn, Nb, Cu, and Ga. The elements Rb, Ba, Zr, Sr, As, Sb, and REE were analyzed at Battelle, Pacific Northwest Laboratories, by sequential INAA using a high-efficiency 130 cm^3 Ge(Li) detector (25% FWHM 1.8 keV for 1332 keV of ^{60}Co), a 4096 channel analyzer, and coincidence-noncoincidence Ge(Li) = NaI (Tl) counting systems (Laul, 1979; Laul et al., 1984). H_2O was determined indirectly by loss on ignition (LOI) at Battelle, Pacific Northwest Laboratories.

Whole-rock F was measured at South Dakota School of Mines and Technology using a fluoride ion-selective electrode technique (Bodkin, 1977), and Fe^{2+} was determined using an HF dissolution and potassium dichromate titration technique of Goldich (1984). Whole-rock Cl was determined at the U.S. Geological Survey, Branch of Geochemistry Laboratory in Menlo Park, California by ion selective electrode (Aruscavage and Campbell, 1983).

XRD procedures and modal determinations

X-ray diffraction, reference intensity method (XRD-RIM) modes were determined by the method described by Shearer et al. (1988).

Finely ground powders were loaded onto Whatman GF/C glass-fiber filters using an aerosol suspension technique that significantly decreases preferred orientation (Davis, 1986). Direct beam X-ray transmission analysis was done on both blank and loaded filters to provide sample mass absorption coefficients. The filters were then mounted in the spinning stage of a Philips diffractometer and scanned from 5 to 60° 2θ using 0.02° steps and 1.5 s count per step (0.8°/min). Monochromatic Cu$K\alpha$ radiation at 40 kv and 20 mA and a graphite monochromator were used for diffraction and transmission scans.

The reference intensity ratio (RIR) method of Chung (1974a, 1974b) modified by Davis (1984) was used for quantitative mineral analysis of the samples. Samples A through H were each mixed with an equal weight of Al_2O_3 (synthetic corundum; a = 4.758 Å, c = 12.991 Å) as an internal standard. Integated peak intensities were adjusted for the use of automatic divergence slits, and the sample mass absorption coefficient was used in adjusting for sample transparency and matrix effects on the loaded filter. Adjusted intensities (I_j) of samples A through H were then used, along with the RIR (k_j), in the relation

$$W_j = \frac{W_c}{I_c} \cdot \frac{I_j}{k_j} \qquad (1)$$

where W_j is the weight fraction of each crystalline component in the sample; W_c and I_c refer to the added weight fraction and integrated intensity of the corundum standard (Chung, 1974a). The addition of an internal standard allows the independent calculation of the weight fraction of each phase; thereby the total amorphous weight fraction can be found by difference. By subtracting the crystalline contribution of the mass absorption from that of the sample, the contribution of one or two amorphous phases may be calculated from the remainder. However, optical studies of the fumarole 212 samples indicate that as many as three amorphous phases (pumice, opal, and limonite) can be present. In that case, one phase must be determined optically from grain mounts, which is usually limonite as it is readily distinguishable from most other phases.

Optical estimates could be made for the crystalline/amorphous ratio for the leached samples J through O,

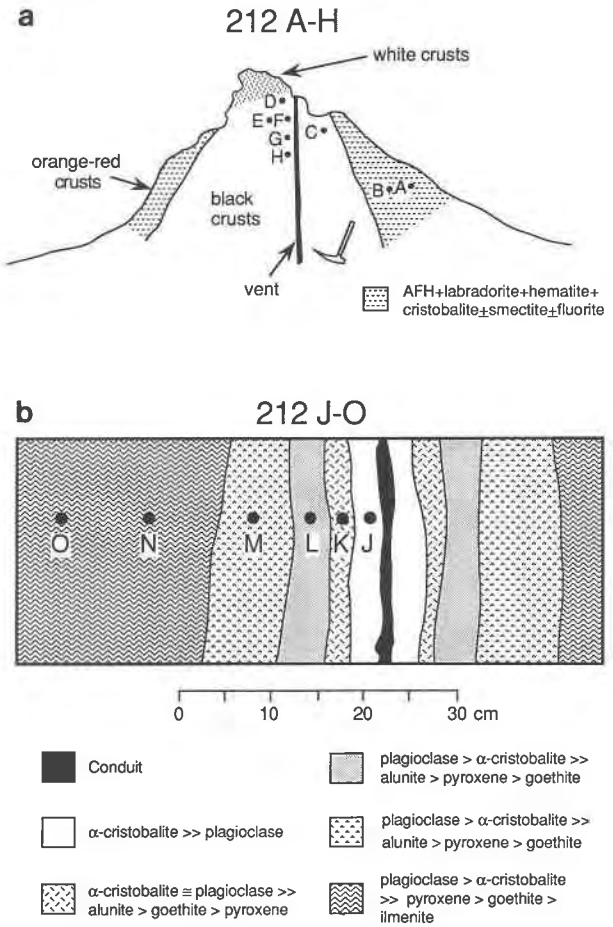

Fig. 3. (**a**) Schematic cross section showing locations of samples from fossil fumarole 212 in the upper, encrusted fallout that overlies the ash-flow tuff of **b**. Geologic hammer indicates scale. (**b**) Schematic map showing location of samples from the ash-flow tuff portion of the fossil fumarole. This section underlies the encrusted fallout deposits of **a**. Crystalline phase assemblages and their relative abundances are indicated. Plagioclase, pyroxene, ilmenite, and some magnetite are primary and in various stages of alteration; α-cristobalite is mostly from devitrification of pumice during high-temperature vapor-phase leaching; alunite and goethite are alteration deposits.

Table 1. XRD modal analyses of 212 traverse

	Crystalline fraction											Amorphous fraction			
Sample	AHF	Alunite	Cristobalite	Fluorite	Hematite	Ilmenite	Goethite	Plagioclase	Magnetite	Pyroxene	Smectite	Total crystal.	Limonite	Obsidian	Opal	Total amorph.
212A	29.09		0.49		0.63			6.34			3.45	40.00	5.60	54.40		60.00
212B	12.59		0.68	1.02	0.87			18.70				33.86	5.15	60.99		66.14
212C			1.49		1.69			18.22		3.85		25.25		61.27	13.49	74.75
212D			1.54		0.89			24.17		1.19	2.20	30.00	4.95	65.05		70.00
212E	1.48		0.32	2.96	2.29			19.41	1.71	1.82		30.00		63.40	6.60	70.00
212F			4.30					15.91			14.79	35.00	3.74	61.26		65.00
212G			1.18		1.16			15.36		2.81	5.11	25.62		72.94	1.44	74.38
212H			0.33		1.64			12.72				14.69		41.85	43.46	85.31
212J			22.95					10.65				33.60	0.80	58.17	7.43	66.40
212K		2.33	17.81				0.57	12.78		0.50		34.00	14.39	51.61		66.00
212L		1.31	12.76				0.35	17.21		1.15		33.00		39.51	26.49	66.00
212M		1.36	12.65				0.55	17.48		0.96		33.00		53.12	12.88	66.00
212N			12.88			0.31	0.49	18.93		1.48		34.10		62.62	3.28	65.90
212O			14.70			0.42	0.57	21.56		2.74		40.00		60.00		60.00

Note: Samples A–H, amorphous phases calculated; J–O amorphous/crystalline ratio estimated optically.

since they contained no isotropic minerals. Therefore the weight fractions for these samples were calculated using a slightly different procedure in which no internal standard is added, but the RIR is used in the relation from Chung (1974b):

$$W_j = \left(\frac{k_j}{I_j}\sum_{i\neq j}^{n}\frac{I_i}{k_i}\right)^{-1}. \quad (2)$$

Further details of both techniques can be found in Davis (1984). All W_j sum to unity, and the relative weight fractions of the crystalline components are correct with respect to the total crystalline fraction of the sample. When one amorphous phase is present, the crystalline/amorphous ratio can be easily determined from the mass absorption coefficient; however, where two or three amorphous phases exist, the ratio is found optically, whereas only the limonite component was optically determined in the previous calculations for samples A through H. The weight fractions of pumice and opal are then calculated by summing the weight fractions of amorphous and crystalline components times their respective mass absorption coefficients such that the total is equal to the measured sample mass absorption coefficient. Modal analyses using a combination of both methods are presented in Table 1.

RIR factors have been tabulated by Davis et al. (1989) for all of the mineral species present except for AHF [$(Al_{16}(F,OH)_{48}\cdot 12\text{–}15\ H_2O)$]. XRD and scanning electron microscope studies show that AHF is complexly intergrown with altered pumice from which it is derived and with other incrustation material; therefore, it is difficult to separate AHF into the pure mineral necessary for RIR measurements. An impure separate of the compound was processed from sample 212A by light crushing and screening and was mixed with an equal weight of corundum. The intensity of the strong XRD peak of AHF was then mathematically corrected for pumice, α-cristobalite, and labradorite impurities present to obtain an RIR measurement of 0.85. Although plagioclase phenocrysts in our samples were in various stages of alteration, microprobe analyses of the freshest samples gave labradorite as a reasonable plagioclase composition to use in our models. Hildreth (1983) determined that in the rhyolite pumice, plagioclase is oligoclase; in dacite pumice, plagioclase ranges in compostion from An_{34} to An_{71} but $An_{36\text{–}53}$ is most common; and in andesite pumice, plagioclase composition ranges from An_{35} to An_{83} with $An_{47\text{–}79}$ the most common. Because of the mixed composition of the ash-flow tuff protolith, a wide range of compositions was probably involved.

Chemical mass balance

Chemical losses and gains resulting from alteration within and adjacent to fossil fumarole 212 were estimated using the isocon method of Grant (1986). This method is a graphical application of Gresens' (1967) procedure. Measured rock densities are not required, an advantage when studying porous pumiceous samples. The chemical data for fossil fumarole 212 samples (encrusted fallout A–H and leached ash-flow tuff J–O) and an unaltered dacite ash-flow tuff protolith sample (VTTS-D) for comparison are presented in Table 2.

Isocon diagrams for selected samples of fumarole 212 are illustrated in Figures 4 and 5. In these diagrams, the concentrations of specific major and trace elements in the original unaltered rock (C_i^O) are plotted against those in the altered rock (C_i^A). If there is no detectable alteration, the data points define a line with a slope of 1, representing constant mass. In most cases, a linear array is defined by some combination of the components (e.g., Al_2O_3, TiO_2, Ga, Y, Zr, Nb, REE, Hf, Ta, Th) commonly considered to be relatively immobile during vapor phase/hydrothermal alteration of volcanic rock (Lesher et al., 1986; Sturchio et al., 1986). This is exemplified in Figures 4 and 5 for samples 212E from the encrusted fallout and 212L from the leached ash-flow tuff. Best-fit isocons to these data arrays were calculated using linear regression analysis (Table 3). The slopes of best-fit isocons, M^O/M^A (mass original/mass altered), were used to assess possible changes

TABLE 2. Chemical compositions of the altered and unaltered dacite-rich protolith of fossil fumarole 212

Sample:	212A	212B	212C	212D	212E	212F	212G	212H	212J	212K	212L	212M	212N	212O	VTTS-D
SiO_2 (wt%)	55.4	57.3	56.3	56.0	57.3	52.6	59.0	59.5	79.3	73.1	68.4	66.1	66.3	66.5	63.5
TiO_2	0.52	0.50	0.70	0.59	0.59	0.55	0.64	0.59	0.61	0.54	0.46	0.50	0.47	0.50	0.61
Al_2O_3	17.2	16.2	16.7	17.6	16.7	18.6	16.9	15.9	6.0	11.6	15.9	16.5	16.0	16.0	16.0
FeO	1.61	1.95	2.63	3.30	2.10	3.12	3.32	3.10	0.71	1.78	2.77	1.60	2.61	1.71	n.a.
Fe_2O_3	2.51	2.24	2.98	3.73	3.57	7.03	1.91	2.95	1.08	<0.02	<0.02	0.46	1.33	1.10	5.60
MnO	0.08	0.07	0.13	0.13	0.11	0.13	0.12	0.12	0.05	0.05	0.07	0.07	0.10	0.08	0.13
MgO	2.2	2.0	3.5	3.1	2.0	2.7	2.2	2.3	1.6	1.5	1.8	1.7	2.1	2.0	2.1
CaO	3.73	5.01	7.11	7.10	6.17	6.72	5.61	5.30	1.66	2.41	3.82	3.85	4.35	4.04	4.95
Na_2O	2.78	2.90	3.00	3.50	3.00	3.53	3.30	3.30	1.61	3.00	3.80	3.70	3.80	3.43	3.85
K_2O	0.89	1.10	0.61	0.70	1.55	1.10	1.30	1.39	1.00	2.12	1.96	1.94	1.90	1.80	1.70
P_2O_5	<0.1	<0.1	<0.1	<0.1	<0.1	<0.1	<0.1	<0.1	<0.1	<0.1	<0.1	<0.1	<0.1	<0.1	<0.1
SO_3	0.42	0.07	0.15	<0.05	<0.05	<0.05	<0.05	<0.05	0.17	0.60	0.34	0.43	<0.05	0.19	<0.05
F	4.89	2.59	1.81	0.66	3.68	1.04	1.22	1.26	0.02	0.03	0.04	0.05	0.04	0.03	0.04
Cl	0.35	0.38	0.24	0.29	0.31	0.12	0.22	0.15	0.57	0.18	0.11	0.07	0.08	0.02	0.077
LOI	7.4	7.6	4.0	4.3	2.9	2.4	4.1	3.2	5.0	3.1	1.7	2.8	0.7	2.7	1.6
O = Cl, Fe	−2.14	−1.18	−0.82	−0.34	−1.62	−0.47	−0.56	−0.56	−0.14	−0.05	−0.04	−0.04	−0.03	−0.02	−0.03
Total	97.84	98.73	99.04	100.66	98.36	99.17	99.28	98.50	99.28	99.96	101.13	99.73	99.75	100.08	100.12
Ba (ppm)	450	470	330	360	510	410	500	510	310	750	720	690	710	640	580
Sr	250	300	360	360	260	320	300	270	80	160	220	240	220	240	260
Zr	106	109	61.8	72.3	129	71.4	130	123	175	154	130	130	130	134	150
Th	2.10	2.26	1.20	1.45	2.80	1.61	2.70	2.60	3.75	4.10	3.60	3.21	3.70	3.60	3.56
Zn	66.3	155	590	200	200	730	440	320	28.5	36.8	43.8	56.6	73.5	48.3	31
Rb	30.0	29.0	13.3	14.4	31.4	54.3	27.6	27.1	24.7	47.0	43.8	36.5	37.8	32.1	36.0
As	530	730	630	130	590	410	110	180	114	66	17.5	24.9	13	18.5	7.0
Cu	20.6	21.7	29.2	23.9	19.9	405	46.2	190	15.2	17.6	19.1	15.0	27.3	14.7	9.3
Ga	14.9	17.4	9.2	14.5	11.4	18.9	14.7	15.4	6.0	11.6	12.1	12.6	15.8	13.6	12.8
Pb	48.3	600	990	280	660	240	160	115	9.3	21.6	19.2	20.5	22.0	11.8	8.0
Br	40.4	41.9	42.7	12.7	48.9	4.3	13.1	4.1	10.2	7.5	3.2	1.3	2.9	<1	<1
Y	33.2	32.3	16.1	18.5	31.6	24.3	24.4	26.5	17.3	20.2	21.8	17.7	27.1	19.4	28.4
Ni	<3	3.2	5.6	10.9	6.4	10.5	7.4	7.4	4.9	5.4	7.6	13.3	10.6	8.3	<4
V	170	200	150	210	160	300	110	155	64	40	40	90	140	170	130
Sn	30	124	106	42	140	52	80	42	16	12	<10	<10	<10	<10	<10
Nb	3.2	3.3	1.9	2.3	4.1	<1.2	3.7	2.9	3.6	3.7	3.1	3.4	3.8	3.2	3.9
Cr	20	20	25	30	20	30	22	20	16	15	20	16	27	17	15.3
Sc	19.0	15.5	26.6	22.7	17.6	23.6	18.9	17.8	11.8	14.2	16.6	17.4	19.1	17.3	20.0
Hf	3.00	3.07	2.00	2.00	3.55	2.30	3.60	3.40	4.80	4.60	4.14	4.02	3.83	3.67	4.13
U	1.1	1.1	0.64	0.70	1.3	0.80	1.3	1.3	1.7	1.9	1.9	1.8	1.8	1.6	1.3
Ta	0.24	0.34	0.30	0.20	0.53	0.16	0.53	0.43	0.35	0.42	0.51	0.32	0.62	0.45	0.33*
Cs	1.77	1.93	1.93	1.60	1.30	13.8	3.70	3.80	0.90	1.70	1.43	1.14	1.16	0.67	1.50
Sb	10.1	15.5	5.6	2.6	3.8	5.3	6.7	3.3	48.0	40.0	2.1	7.1	1.3	7.3	0.75
Au**	<5.0	<5.0	<5.0	<5.0	3.5	40	7.0	15	10	<5.0	<5.0	<5.0	8.0	10	<3
Co	6.20	5.30	12.9	18.9	10.5	22.0	14.6	16.9	6.20	7.90	12.1	23.5	14.0	25.8	n.a.
La	11.7	12.0	6.88	7.90	11.4	9.47	10.7	11.3	5.35	10.2	11.4	10.1	11.2	9.05	12.7
Ce	27.0	25.4	15.1	18.1	26.0	20.7	24.3	25.4	11.1	20.0	22.9	19.1	24.0	17.3	30.4
Nd	19.2	18.0	10.0	11.8	17.2	15.0	16.6	16.8	7.0	11.5	12.6	10.0	14.0	10.0	20.7
Sm	5.40	4.86	2.65	3.02	4.57	4.00	3.91	4.20	1.4	2.55	2.76	2.30	3.50	2.26	4.40
Eu	1.70	1.50	1.12	1.10	1.18	1.24	1.10	1.06	0.40	0.77	0.96	0.87	0.99	0.84	1.15
Gd	6.6	6.6	3.6	3.9	5.7	5.5	4.8	5.6	3.0	3.4	3.6	3.0	4.4	3.0	5.4
Tb	1.10	1.02	0.65	0.66	1.03	0.90	0.86	0.84	0.47	0.62	0.62	0.52	0.78	0.50	1.00
Ho	1.5	1.1	0.7	1.0	1.4	1.2	1.2	1.3	0.82	1.1	1.0	0.88	1.3	0.90	1.3
Tm	0.53	0.57	0.38	0.34	0.48	0.42	0.42	0.43	0.35	0.36	0.42	0.38	0.50	0.34	0.51
Yb	3.70	3.45	2.10	2.30	3.25	2.80	2.81	2.85	2.31	2.35	2.82	2.20	3.16	2.37	3.40
Lu	0.54	0.53	0.32	0.34	0.49	0.41	0.43	0.43	0.35	0.37	0.44	0.35	0.48	0.36	0.53

Note: n.a. = not analyzed.
* Ta value for Hildreth (1983).
** Au in ppb.

in rock mass that occurred during alteration. Isocon slopes for samples A–H in the encrusted fallout and J, N, and O in the leached tuff deviate very little from 1 (Table 3), indicating that rock mass was essentially conserved during alteration processes. The isocon slopes for samples K, L, and M correspond to mass increases of 20%, 16%, and 14%, respectively.

The gains and losses of major oxides, F and LOI ($\sim H_2O$), calculated for the two chemical profiles documented in Table 2 are reported in Table 4. The mass exchange detemined for major oxides approximates the mass exchange indicated by the isocons. This is an independent check on the method because the slope of the isocon is based on immobile trace elements, not entirely on major oxides. The values reported in Table 4, along with the results of trace-element mass balance calculations, are normalized to the original unaltered rock content of each component and presented on enrichment-depletion diagrams in Figure 6. These diagrams illustrate that for samples A–H: SO_3, F, LOI ($\sim H_2O$), Cl, Zn, As, Cu, Pb, Br, Ni, V, Sn, Cr, Cs, Sb, and Au are enriched, and SiO_2, Na_2O, K_2O, Zr, U, Th, Ba, and Rb are depleted. Total Fe as Fe_2O_3, MnO, MgO, CaO, Sr, and Sc generally show erratic and insignificant variations. Along the

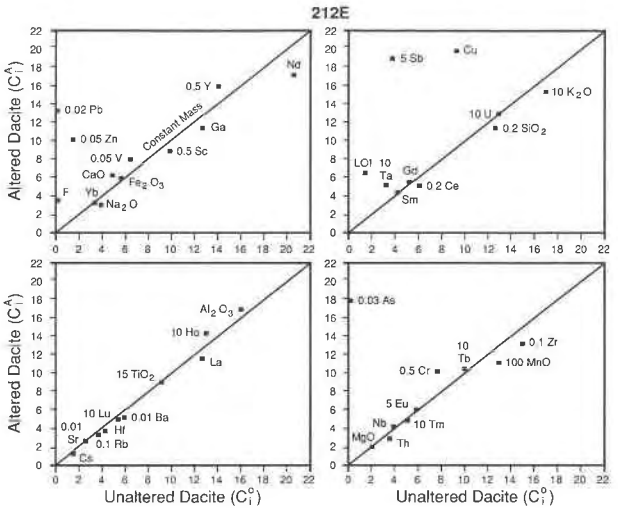

Fig. 4. Isocon diagram for sample 212E showing an example of constant mass relationships in the encrusted fallout part of the fossil fumarole. Isocon diagrams plotted according to the method of Grant (1986). Major oxides in weight percent; trace elements in ppm except Au in ppb. Numbers above components are factor used to bring component concentration in unaltered rhyolite onto range of isocon so that enrichment or depletion can be determined, e.g., 10 K_2O has original concentration of 1.55 wt% (Table 2) and plots at $10 \times 1.55 = 15.5$ on the y axis.

chemical profile of the leached ash-flow tuff, J–O, SiO_2, SO_3, LOI (~H_2O), Zn, As, Cu, Pb, Br, Ni, Sn, Cr, U, Sb, and Au are enriched and Fe_2O_3, MnO, CaO, and V are depleted. Al_2O_3, CaO, Na_2O, K_2O, F, Ba, Sr, Rb, Ga, Y, Sc, and Cs are significantly depleted in the most intensely altered sample, J, which is the sample immediately adjacent to the fumarole conduit in the ash-flow tuff and therefore subject to the greatest interaction between fluid and rock.

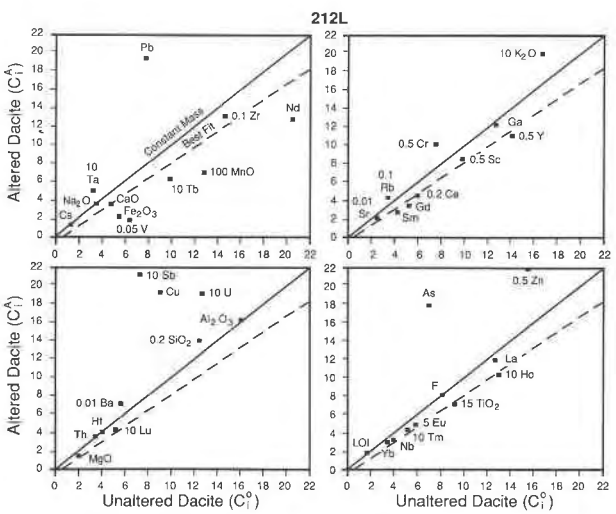

Fig. 5. Isocon diagram for sample 212L showing an example of mass gain in the leached ash-flow tuff part of the fossil fumarole. Explanation as for Figure 4.

Table 3. Isocon definitions

Sample	R	M^o/M^A	Isocon components*
A	0.981	0.99	Al, Ti, Nb, La, Ce, Nd, Sm, Gd, Tb, Tm, Yb, Lu, Hf, Ta, Th
B	0.976	0.96	Al, Ti, Y, Nb, La, Ce, Nd, Sm, Gd, Tb, Tm, Yb, Lu, Hf, Ta, Th
C	0.995	1.07	Al, Ti, Ta
D	N.A.	0.97	Ti
E	0.987	1.05	Al, Ti, Ga, Y, Nb, La, Ce, Sm, Gd, Tb, Ho, Tm, Yb, Lu, Hf, Th, U
F	0.995	0.93	Ti, Sm, Gd, Tb, Ho, Tm, Yb
G	0.992	1.07	Al, Ti, Nb, Ce, Sm, Gd, Tb, Ho, Tm, Yb, Lu, Hf, Th, U
H	0.990	1.01	Al, Ti, Y, Nb, Ce, Sm, Gd, Tb, Ho, Tm, Yb, Lu, Hf, Ta, Th, U
J	0.992	0.99	Ti, Cr, Nb, Hf, Ta, Th
K	0.977	0.80	Al, Ti, Y, La, Ce, Sm, Gd, Tb, Ho, Tm, Yb, Lu
L	0.978	0.84	Ti, Y, Zr, Nb, La, Ce, Sm, Gd, Tb, Ho, Tm, Yb, Lu
M	0.979	0.86	Ti, Zr, Nb, La, Ce, Sm, Gd, Ho, Tm, Yb, Lu
N	0.989	0.98	Al, Ti, Y, Nb, La, Ce, Sm, Gd, Ho, Tm, Yb, Lu, Hf, Th
O	0.983	1.00	Al, Ti, Ga, Nb, Hf, Ta, Th

Note: R = correlation coefficient; M^o/M^A = isocon slope; N.A. = not applicable.

* Elements used to define isocons.

REE SIGNATURES

Eleven REE were determined for 14 samples from fumarole 212 and for a sample of unaltered dacite pumice (VTTS-D) (Table 2). Hildreth (1983, p. 34) presented REE data for unaltered rhyolite, dacite, and andesite pumice samples and high-purity glass separates. The fumarolically encrusted dacite-rich fallout samples (A–H; Fig. 7) show variable REE patterns indicating redistribution as a result of fumarolic alteration. Samples E and H are similar to the dacitic protolith; samples F and G are less so. However, samples A, B, C, and D illustrate some total REE depletions and, more significantly, positive Eu anomalies. Michard (1989) has shown that chondrite-normalized REE concentrations of high-temperature acidic H_2O ($pH < 6$; $T > 230$ °C) have high positive Eu anomalies. Thus a reasonable interpretation of the positive Eu anomaly is that Eu^{2+} has been mobilized and enriched relative to the trivalent REE. Hot acidic solutions transported Eu^{2+} preferentially to the other REE and deposited it in the more altered samples.

REE patterns in fossil fumaroles in rhyolite-rich protolith (fumaroles 63 and 64) in the lower VTTS (Papike et al., 1991) indicate that high-temperature fumarolic alteration that cooled rapidly and was not subjected to surficial acid alteration resulted in a small amount of REE movement except for Eu (fumarole 64). However, fumarole 63, which was subjected to extensive acid alteration, showed highly variable REE values and especially enrichment of Eu in altered samples relative to unaltered rhyolite pumice. Thus REE pattern disturbances might be an effective means of evaluating the degree of alteration of VTTS fumarolic incrustations, particularly the effect of acid alteration.

In samples J–O (Fig. 8) from the leached ash-flow sheet,

the most altered sample (J) adjacent to the fumarole conduit shows Eu depletion that is consistent with the significant loss of plagioclase by high-temperature fumarolic leaching (Table 1, Fig. 9). Sample O, which has the highest modal plagioclase (21%, Table 1) and is the least altered, has the geatest positive Eu anomaly. Hildreth (1990, and personal communication) suggests that an additional factor that may cause variable REE concentrations and, specifically, Eu^{2+} is mechanical sorting of plagioclase during tephra deposition.

Discussion

Interpretation of fossil fumarole mineralogy and geochemistry is complicated by weathering superimposed on the complex leaching and depositional processes of active fumarolic evolution from high-temperature vapor-phase processes through cooling processes. In addition, the complex fine-grained intergowths and thin depositional coatings of sublimates and secondary minerals superimposed upon primary glasses and phenocrysts in various stages of alteration (depending upon position in the area affected by the fumarole) make the interpretations of the data difficult. An additional consideration of the complexity of the system is that during fumarolic activity, a substantial volume of unstable compounds, which contain as much as several weight percent of trace metals, are formed (Keith et al., 1981, 1989). These compounds include chlorides and sulfates of all the major constituents except Ti and many minor elements (Shipley, 1920; Keith, 1991). Therefore, substantial amounts of elements leached by fumarolic gases are removed from the area by dissolution within hours and days of deposition (Keith et al., 1989). As fumaroles cool and die out, late-stage minerals are deposited in pore spaces where earlier leaching occurred.

Given that this study is based on bulk samples rather than discrete mineral phases, we are of the opinion that our study provides unique understanding of the bulk chemical leaching and depositional processes in high-temperature fumaroles at the VTTS. Caution must be used in assessing rock masses and associated chemical gains and losses in these bulk samples because both leaching and deposition have occurred in many places because of the processes described above. Also the composition used for original protolith is only an approximation.

To understand the chemical systematics of our results, the mineral assemblages and alteration textures must be considered. The major mineral modal analyses along with some of the chemical data are illustrated in Figure 10. Crystalline phases introduced in the alteration assemblages by fumarolic alteration and subsequent cooling reactions include alunite reflecting high SO_3 activity; AHF and fluorite reflecting high F activity; smectite, magnetite, hematite, and goethite reflecting oxidation and hydration; and opal and some of the α-cristobalite reflecting SiO_2 mobility. Although the encrusted fallout (A–H) shows great chemical and mineralogical diversity, the leached ash-flow tuff (J–O) shows some systematics. For the leached part of the system (note Fig. 9), the modal data and thin sections show that plagioclase, pyroxene, magnetite, and ilmenite phenocrysts are removed adjacent to the fumarole conduit and are less altered away from the conduit. The abundance of α-cristobalite increases toward the conduit.

Comparing the chemical data shown on Figures 6 and 10, substantial enrichments in some elements occur in encrusted fallout samples A–H compared to the leached ash-flow, e.g., Zn, Cu, F, Cl, CaO, Fe_{tot} as Fe_2O_3. Also, note the enrichments are localized, particularly in samples F and C. The F enrichments clearly correlate with increases in AHF and fluorite in sample A. Although the associated mineralogy does not always indicate where these enriched elements might be concentrated, referring to Figure 3a, the most enriched samples come from the near surface part of the system and near the conduit where these elements would have been sublimated from fumarolic fluids. Although primary dacite-rich fall clasts remain in various stages of alteration in the encrusted fallout, certain elements are clearly enriched over the content of the primary clasts, i.e., dacite protolith.

Overall chemical relationships illustrated in Figure 6 are determined as follows:

1. The sample adjacent to the conduit, J, is heavily leached of most elements except LOI ($\sim H_2O$), Cl, SiO_2, SO_3, Zr, As, Au, Sb, Cu, Pb, Ni, Cr, Hf, and U.
2. Leached from the ash-flow tuff and deposited in the fallout or deposited directly from the volcanic vapor phase are Fe_2O_3, MgO, CaO, Cl, F, Sr, V, Sc, and Cs.
3. Relatively enriched in the leached ash-flow tuff and depleted in the fallout are SiO_2, K_2O, Ba (except adjacent to the conduit were it is strongly depleted), Zr, Th, Rb, Hf, U, and Ta.
4. Enriched in both parts of the fossil fumarolic system are SO_3, LOI ($\sim H_2O$), F, Zn, As, Cr, Pb, Br, Ni, Sn, Sb, and Au. Al_2O_3 and Ga are slightly enriched in both parts of the system except for strong depletion adjacent to the conduit in the leached ash-flow tuff.
5. Depleted in both parts of the system are Na_2O, MnO, Y, Nb, and REE.
6. TiO_2 is close to constant in both parts of the system but is slightly enriched or depleted in individual samples without any pattern indicating that it is relatively stable under the various conditions that have affected this fossil fumarole. The variability is most likely a result of variable protolith composition.

The enrichments and depletions are similar to those for fumarolically altered and incrusted tephra in the distal, rhyolite-rich part of the ash-flow sheet (Papike et al., 1991). Major oxides and trace elements enriched in fossil fumarolic incrustations in both the dacite-rich protolith (fumarole 212) and the rhyolite-rich protolith (fumaroles 63, 64, 69; Papike et al., 1991) are Fe_2O_3, MgO, CaO, SO_3 (except 64), LOI ($\sim H_2O$), Sr, Zn, Cu, Br, and F. In addition, enrichments in incrustations from fumarole 212 and at least one rhyolite-rich protolith fumarole are Ni, Cr, As, Au, Sn, and Pb. Depletions of Na_2O occur in all

TABLE 4. Compositional gains and losses compared to 100 g of unaltered dacite

	Encrusted dacite-rich fallout								
	A	B	C	D	E	F	G	H	Average
SiO_2	−8.1	−6.2	−7.2	−7.5	−6.2	−10.9	−4.5	−4.0	−6.8
TiO_2	−0.09	−0.11	0.09	−0.02	−0.02	−0.06	0.03	−0.02	−0.03
Al_2O_3	1.2	0.2	0.7	1.6	0.7	2.6	0.9	−0.1	1.0
Fe_2O_3	−1.30	−1.20	0.30	1.80	0.30	4.90	0.00	0.80	0.70
MnO	−0.05	−0.06	0.00	0.00	−0.02	0.00	−0.01	−0.01	−0.02
MgO	0.10	−0.10	1.40	1.00	−0.10	0.60	0.10	0.20	0.40
CaO	−1.22	0.06	2.16	2.15	1.22	1.77	0.66	0.35	0.89
Na_2O	−1.07	−0.95	−0.85	−0.35	−0.85	−0.32	−0.55	−0.55	−0.69
K_2O	−0.81	−0.06	−1.09	−1.00	−0.15	−0.60	−0.40	−0.31	−0.55
SO_3	0.37	0.02	0.10	0.00	0.00	0.00	0.00	0.00	0.06
F	4.85	2.55	1.77	0.62	3.64	1.00	1.18	1.22	2.10
LOI	5.8	6.0	2.4	2.7	1.3	0.8	2.5	1.6	2.9
Mass change	−0.32	0.15	−0.22	1.00	−0.18	−0.21	−0.09	−0.82	−0.09

four fossil fumaroles. Although the masses of individual components moved in fumaroles in different protoliths vary, the similarities in the chemical species that are enriched and depleted suggests that the fumarolic gas composition is the most critical factor in determining which components are moved, regardless of protolith.

Comparison with Symonds et al. (1987), who report enrichment in sublimates and incrustation in most elements for high-temperature (500–800 °C) fumaroles at Merapi volcano, shows that the same suite of enriched components occur in both the leached ash-flow tuff and the encrusted fallout at fossil fumarole 212 in the VTTS.

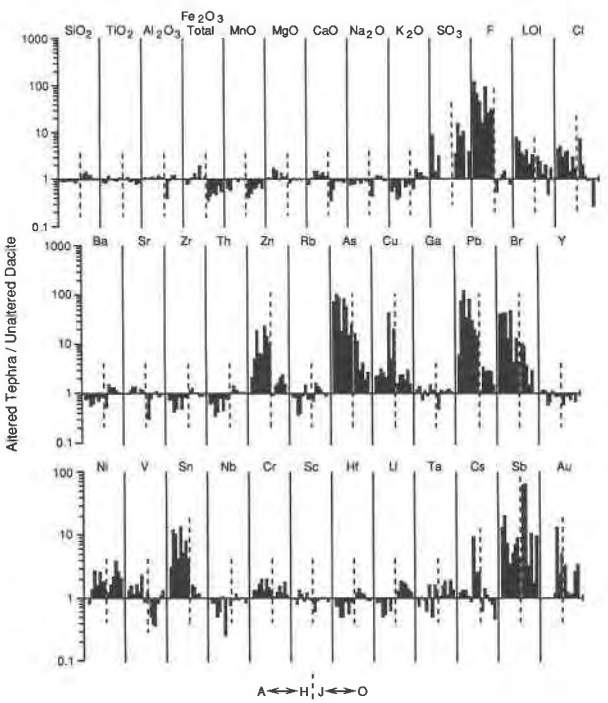

Fig. 6. Enrichment and depletion diagram for fumarole 212. Samples A–H are from the encrusted fallout part of the fossil fumarole; locations as in Figure 3a. Samples J–O are from the leached ash-flow tuff as shown in Figure 3b with J, adjacent to the fumarole conduit, being the most leached.

Thus we conclude that in both parts of the fossil fumarole we are dealing with the shallow part of the fumarole system. The most visible component, Fe_2O_3, along with MgO, CaO, Cl, F, Sr, V, Sc, and Cs, was leached from the ash-flow sheet and deposited in the fallout (Fig. 6). The com-

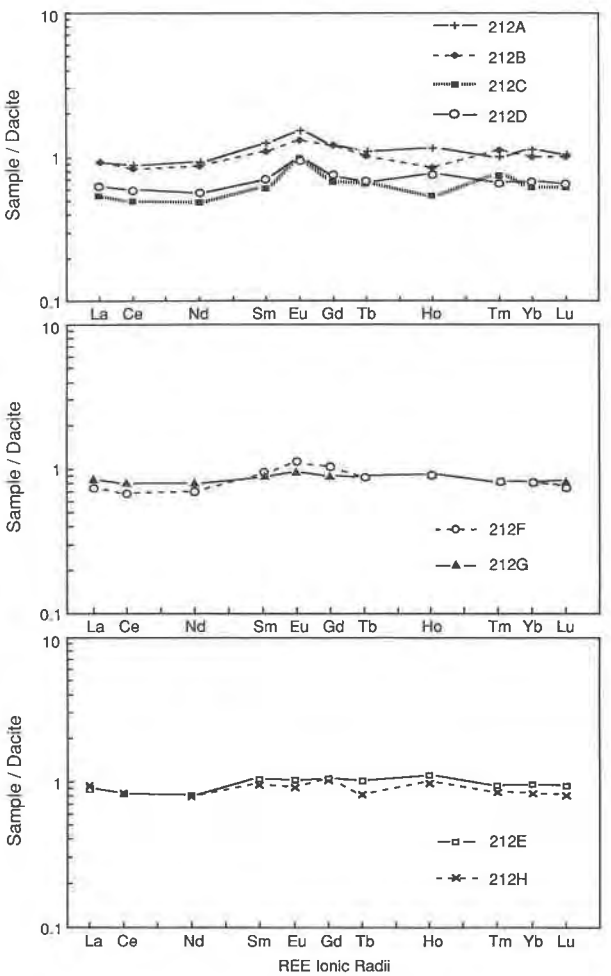

Fig. 7. REE patterns for samples from the encrusted fallout part of fumarole 212 normalized against dacite protolith REE concentrations.

TABLE 4—*Continued*

	Leached dacite-rich ash-flow tuff						
	J	K	L	M	N	O	Average
SiO_2	15.8	27.9	17.9	13.4	2.8	3.0	13.5
TiO_2	0.00	0.06	−0.06	−0.03	−0.14	−0.11	−0.05
Al_2O_3	−10.0	−1.5	2.9	3.2	0.0	0.0	−0.9
Fe_2O_3	−3.73	−3.15	−2.71	−3.00	−1.37	−2.60	−2.76
MnO	−0.08	−0.07	−0.05	−0.05	0.05	−0.05	−0.04
MgO	−0.50	−0.22	0.04	−0.12	0.00	−0.10	−0.15
CaO	−3.29	−1.94	−0.40	−0.47	−0.60	−0.91	−1.27
Na_2O	−2.24	−0.10	0.67	0.45	−0.05	−0.42	−0.28
K_2O	−0.70	0.95	0.63	0.56	0.20	0.10	0.29
SO_3	0.12	0.70	0.35	0.45	0.00	0.14	0.29
F	−0.02	0.00	0.01	0.02	0.00	−0.01	0.00
LOI	3.4	2.3	0.4	1.7	−0.9	1.1	1.3
Mass change	−1.18	24.9	19.7	16.1	0.00	0.15	9.95

ponents enriched in both parts of the system were transported during high-temperature fumarolic alteration but also during cooling processes and became fixed in more stable solids so as to be resistant to further alteration. As, Sb, and Au are a well-known association in shallow epithermal deposits (White and Heropoulos, 1983; Hedenquist and Henley, 1985; Berger, 1985; Romberger, 1988). Pb, Zn, and Cu are also a common association in shallow parts of epithermal systems and volcanic exhalative deposits (Sillitoe and Bonham, 1984; Berger, 1985). Sn and F are a common association in high-silica rhyolites that yield cassiterite ore deposits (Burt and Sheridan, 1987; Duffield, 1990). SO_3 and H_2O are added during cooling and acid alteration.

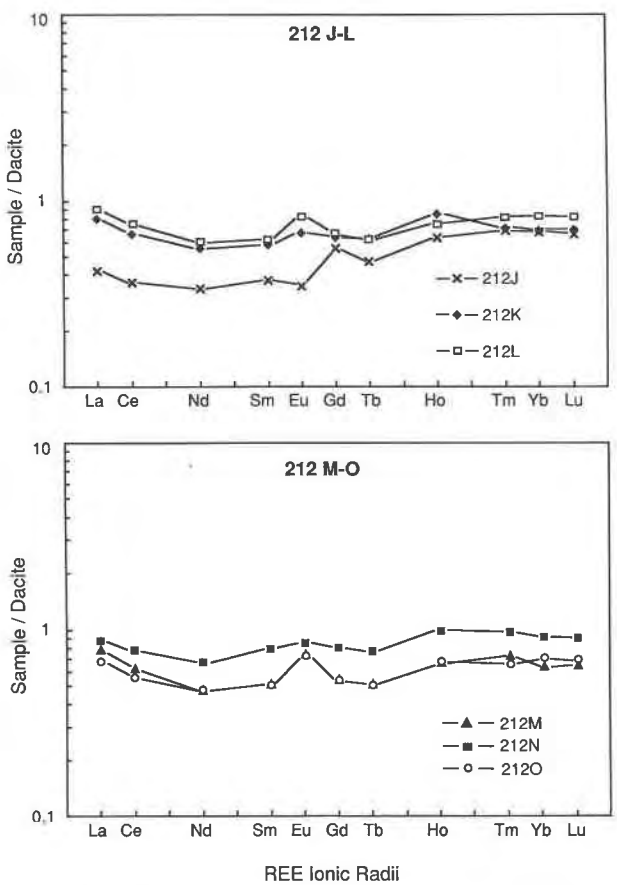

Fig. 8. REE patterns for samples from the leached ash-flow tuff part of fumarole 212 normalized against dacite protolith REE concentrations.

CONCLUSIONS

This study looked at the upper part of a fossil fumarolic system in which ash-flow tuff of mixed rhyolitic, dacitic, and andesitic pumice was leached by high-temperature fluids that carried chemicals upward, where they were sublimated onto permeable dacite-rich fallout and subjected to further alteration, particularly surficial acid alteration, as the fumarole cooled and died out.

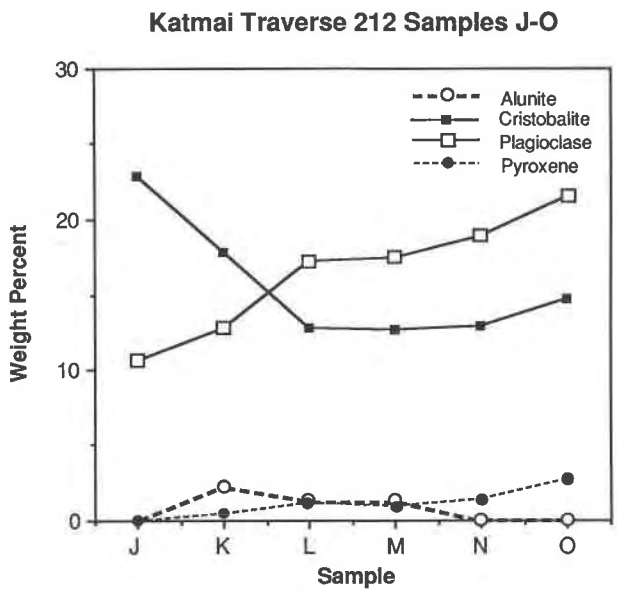

Fig. 9. Variation of modal proportions of crystalline phases from the conduit (sample J) outward in the lower, leached ash-flow tuff part of the system. Depletion of plagioclase and pyroxene from high-temperature vapor-phase and later hydrothermal alteration and crystallization of α-cristobalite from altered pumice adjacent to the conduit are clearly demonstrated.

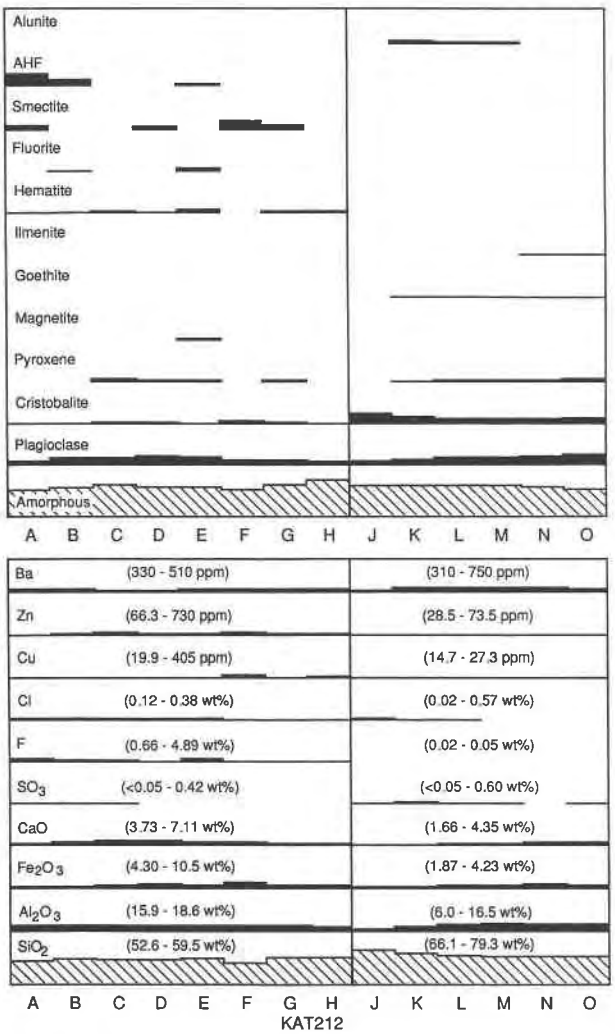

Fig. 10. Schematic modal and selected chemical data for fumarole 212. Samples A–H are from the encrusted fallout part of the fossil fumarole; samples J–O are sequentially outward from the leached fumarolic conduit in the ash-flow tuff. Chemical data in parentheses are taken from Table 2. Relative thickness of bars represents relative abundance of phase in upper part of diagram and abundance of selected major oxides and trace elements in lower part.

Studies of mineralogy and chemical composition of whole-rock samples of fossil fumarole 212 show important characteristics for understanding and interpreting fossil fumarolic systems. These studies address the entire sequence of alteration processes from high-temperature, vapor-phase fumarolic alteration through cooling processes during which fumarolic minerals and their chemical constituents are subjected to secondary alteration. Finally, they also record weathering processes that include dissolution of unstable and metastable deposits.

This study illustrates the usefulness of the isocon method of Grant (1986) to interpret a complex alteration system, providing that the geologic constraints are carefully evaluated.

Acknowledgments

This research was funded by NSF grant EAR-8907712 (J.J.P.), the U.S. Geological Survey (T.E.C.K.), and DOE Contract DE-AC06-76RLO-1830 (J.C.L.). We gratefully acknowledge this support. We thank D. Tully for collecting much of the XRD data.

References cited

Allen, E.T., and Zies, E.G. (1923) A chemical study of fumaroles of the Katmai region. National Geographic Society, Contributed Technical Papers, Katmai Series, 2, 75–155.

Aruscavage, P.J., and Campbell, E.Y. (1983) An ion-selective electrode method for the determination of Cl in geological materials. Talanta, 30, 745–749.

Berger, B.R. (1985) Geologic-geochemical features of hot-spring precious-metal deposits. U.S. Geological Survey Bulletin, 1646, 47–53.

Bodkin, J.B. (1977) Determination of fluorine in silicates by use of an ion-selective electrode following fusion with lithium metaborate. The Analyst, 102, 409–413.

Burt, D.M., and Sheridan, M.F. (1987) Types of mineralization related to fluorine-rich silicic lava flows and domes. Geological Society of America Special Paper 212, 103–109.

Chung, F.H. (1974a) Quantitative interpretation of X-ray diffraction patterns of mixtures. 1. Matrix-flushing method for quantitative multicomponent analysis. Journal of Applied Crystallography, 7, 519–525.

——— (1974b) Quantitative interpretation of X-ray diffraction patterns of mixtures. II. Adiabatic principle of X-ray diffraction analysis of mixtures. Journal of Applied Crystallography, 7, 526–531.

Curtis, G.H. (1968) The stratigraphy of the ejecta from the 1912 eruption of Mount Katmai and Novarupta, Alaska. Geological Society of America Memoir 116,153–210.

Davis, B.L. (1984) Reference intensity quantitative analysis using thin-layer aerosol samples. Advances in X-ray Analysis, 27, 339–348.

——— (1986) A tubular aerosol suspension chamber for the preparation of powder samples for X-ray diffraction analysis. Powder Diffraction, 1, 240–243.

Davis, B.L., Smith, D.K., and Holomany, M.A. (1989) Tables of experimental reference intensity ratios, Table no. 2, December, 1989. Powder Diffraction, 4, 201–205.

Desborough, G.A., and Rostad, 0. (1980) Hydrated aluminum hydroxyfluoride, a ralstonite-like mineral at Big Southem Butte, Snake River Plain, Idaho. American Mineralogist, 65, 1057–1058.

Duffield, W.A. (1990) Eruptive fountains of silicic magma and their possible effects on the tin content of fountain-fed lavas, Taylor Creek Rhyolite, New Mexico. Geological Society of America Special Paper 246, 251–261.

Eichelberger, J.C., and Hildreth, W. (1986) Research drilling at Katmai, Alaska. Eos, 67, 778–780.

Fierstein, J., and Hildreth, W. (1990) Contemporaneity of pyroclastic flows and falls; evidence from the eruption at Novarupta (Alaska) in 1912. Eos, 71, 1690.

Flanagan, F.J. (1967) U.S. Geological Survey rock standards, Geochimica et Cosmochimica Acta, 31, 289–308.

——— (l969) U.S. Geoloaical Survey standards—II. First compilation of data for the new U.S.G.S. rocks. Geochimica et Cosmochimica Acta, 33, 81–120.

——— (1973) 1972 values for international geochemical reference samples. Geochimica et Cosmochimica Acta, 37, 1189–1200.

Goldich, S.S. (1984) Determination of ferrous iron in silicate rocks. Chemical Geology, 42, 343–347.

Grant, J.A. (1986) The isocon diagram—A simple solution to Gresens' equation for metasomatic alteration. Economic Geology, 81, 1976–1982.

Gresens, R.L. (1967) Compositional-volume relationships of metasomatism. Chemical Geology, 2, 47–65.

Griggs, R.F. (1922) The Valley of Ten Thousand Smokes, 340 p. National Geographic Society, Washington, DC.

Hedenquist, J.W., and Henley, R.W. (1985) Hydrothermal eruptions in the Waiotapu geothermal system, New Zealand: Their origin, associated breccias, and relation to precious metal mineralization. Economic Geology, 80, 1640–1668.

Hildreth, W. (1983) The compositionally zoned eruption of 1912 in the Valley of Ten Thousand Smokes, Katmai National Park, Alaska. Journal of Volcanology and Geothermal Research, 18, 1–56.

——— (1987) New perspectives on the eruption of 1912 in the Valley of Ten Thousand Smokes, Katmai National Park, Alaska. Bulletin of Volcanology, 49, 680–693.

——— (1990) The Katmai eruption of 1912: Was the magma stored beneath Novarupta, Trident or Mount Katmai? Petrochemical and temporal evidence. Eos, 71, 1691.

Keith, T.E.C. (1983) Mineralogical and chemical changes in fumarolic deposits with time at surface conditions, p. 231–234. Fourth International Symposium on Water-Rock Interaction, Proceedings, Misasa, Japan.

——— (1984) Preliminary observations on fumarole distribution and alteration, Valley of 10,000 Smokes, Alaska. U.S. Geological Survey Circular 939, 82–85.

——— (1991) Fossil and active fumaroles in the 1912 eruptive deposits, Valley of Ten Thousand Smokes, Alaska. Journal of Volcanology and Geothermal Research, 45, 227–254.

Keith, T.E.C., Casadevall, T.C., and Johnston, D.A. (1981) Fumarole encrustations: Occurrence, mineralogy, and chemistry. U.S. Geological Survey Professional Paper 1250, 239–250.

Keith, T.E.C., Heropoulos, C., and Presser, T.S. (1989) Chemical transport during fumarolic alteration, cooling, and weathering, Valley of Ten Thousand Smokes, Alaska, p. 377–379. Proceedings, Sixth International Symposium on Water-Rock Interaction. Malvern, England.

Kienle, J. (1970) Gravity traverses in the Valley of Ten Thousand Smokes, Katmai National Monument, Alaska. Journal of Geophysical Research, 75, 6641–6649.

Kodosky, L., and Keskinen, M. (1990) Fumarole distribution, morphology, and encrustation mineralogy associated with the 1986 eruptive deposits of Mount St. Augustine, Alaska. Bulletin of Volcanology, 52, 175–185.

Laul, J.C. (1979) Neutron activation analysis of geological materials. Atomic Energy Review, 17.3, 603–695.

Laul, J.C., Walker, R.J., Shearer, C.K., Papike, J.J., and Simon, S.B. (1984) Chemical migration by contact metamorphism between pegmatite and country rock: Natural analogs for radionuclide migration. Materials Research Society Symposium Proceedings, 26, 951–958.

Lesher, C.M., Gibson, H.L., and Campbell, I.H. (1986) Composition-volume changes during hydrothermal alteration of andesite at Buttercup Hill, Noranda District, Quebec. Geochimica et Cosmochimica Acta, 50, 2693–2705.

Lovering, T.S. (1957) Halogen-acid alteration of ash at Fumarole No. 1, Valley of Ten Thousand Smokes, Alaska. Geological Society of America Bulletin, 68, 1585–1604.

Michard, A. (1989) Rare earth element systematics in hydrothermal fluids. Geochimica et Cosmochimica Acta, 53, 745–750.

Papike, J.J., Spilde, M.N., Galbreath, K.C., Shearer, C.K., Keith, T.E.C., and Laul, J.C. (1989) Geochemistry and mineralogy of fumarole deposits, Valley of Ten Thousand Smokes, Alaska: Reference intensity method (RIM) XRD modal analysis. Eos, 70, 1412–1413.

——— (1990a) Geochemistry and mineralogy of fumarole deposits, Valley of Ten Thousand Smokes, Alaska: Alteration of rhyolite ash-flow tuff protolith. Second V.M. Goldschmidt Conference, Baltimore, Maryland, Abstracts with Programs, 72.

——— (1990b) Geochemistry and mineralogy of fumarole deposits, Valley of Ten Thousand Smokes (VTTS), Alaska: Bulk chemical and mineralogical evolution of a dacitic fissure fumarole. Geological Society of America Abstracts with Programs, A351–A352.

Papike, J.J., Spilde, M.N., Shearer, C.K., and Keith, T.E.C. (1990c) Geochemistry and mineralogy of fumarole deposits, Valley of Ten Thousand Smokes (VTTS), Alaska: Major element mass exchange and trace element enrichment/depletion systematics. Eos, 71, 1690–1691.

Papike, J.J., Keith, T.E.C., Spilde, M.N., Galbreath, K.C., Shearer, C.K., and Laul, J.C. (1991) Major and trace element mass flux in fumarolic deposits, Valley of Ten Thousand Smokes, Alaska: Rhyolite-rich protolith. Geophysical Research Letters, in press.

Quisefit, J.P., Toutain, J.P., Bergametti, G., Javoy, M., Cheynet, B., and Person, A. (1989) Evolution versus cooling of gaseous volcanic emission from Monotombo Volcano, Nicaragua: Thermochemical model and observations. Geochimica et Cosmochimica Acta, 53, 2591–2608.

Ramdohr, P. (1962) Erzmikroskopische unersuchungen an magnetiten der exhalationen im Valley of the 10 000 Smokes. Neues Jahrbuch für Mineralogie Monatshefte, 3/4, 49–59.

Romberger, S.B. (1988) Geochemistry of gold in hydrothermal deposits. U.S. Geological Survey Bulletin, 1857-A, A9–A25.

Shearer, C.K., Papike, J.J., Simon, S.B., Davis, B.L., and Laul, J.C. (1988) Mineral reactions in altered sediments from the California State 2-14 Well: Variations in the modal mineralogy, mineral chemistry and bulk composition of the Salton Sea Scientific Drilling Project Core. Journal of Geophysical Research, 93, 13104–13122.

Shipley, J.W. (1920) Some chemical observations on the volcanic emanations and incrustations in the Valley of 10,000 Smokes, Katmai, Alaska. American Journal of Science, 50, 141–153.

Sillitoe, R.H., and Bonham, H.F., Jr. (1984) Volcanic landforms and ore deposits, Economic Geology, 79, 1286–1298.

Stoiber, R.E., and Rose, W.I., Jr. (1974) Fumarole incrustations at active Central American volcanoes. Geochimica et Cosmoschimica Acta, 38, 495–516.

Sturchio, N.C., Muehlenbachs, K., and Seitz, M.G. (1986) Element redistribution during hydrothermal alteration of rhyolite in an active geothermal system: Yellowstone drill cores Y-7 and Y-8. Geochimica et Cosmochimica Acta, 50, 1619–1631.

Symonds, R.B., Rose, W.I., Reed, M.H., Lichte, F.E., and Finnegan, D.L. (1987) Volatilization, transport and sublimation of metallic and nonmetallic elements in high temperature gases at Merapi Volcano, Indonesia. Geochimica et Cosmochimica Acta, 51, 2083–2101.

Symonds, R.B., Rose, W.I., Gerlach, T.M., Briggs, P.H., and Harmon, R.S. (1990) Evaluation of gases, condensates, and SO_2 emissions from Augustine volcano, Alaska: The degassing of a Cl-rich volcanic system. Bulletin of Volcanology, 52, 355–374.

White, D.E., and Heropoulos, C. (1983) Active and fossil hydrothermal-convection systems of the Great Basin. Geothermal Resources Council Special Report 13, 41–53.

Zies, E.G. (1929). The Valley of Ten Thousand Smokes: I. The fumarolic incrustations and their bearing on ore deposition. II. The acid gases contributed to the sea during volcanic activity. National Geographic Society, Contributed Technical Papers, Katmai Series, 4, 1–79.

Manuscript received June 18, 1990
Manuscript accepted May 20, 1991